Relationship between structural coherence and intrinsic carrier transport in an isolated poly(3-hexylthiophene) nanofiber

Takeshi Shimomura,[1,*] Tomoyuki Takahashi,[1] Yasutaka Ichimura,[1] Shino Nakagawa,[1] Keiichi Noguchi,[2] Seiji Heike,[3] and Tomihiro Hashizume[3]

[1]*Graduate School of Bio-Applications and Systems Engineering, Tokyo University of Agriculture and Technology, Koganei, Tokyo 184-8588, Japan*

[2]*Instrumentation Analysis Center, Tokyo University of Agriculture and Technology, Koganei, Tokyo 184-8588, Japan*

[3]*Advanced Research Laboratory, Hitachi Ltd., Hatoyama, Saitama 350-0395, Japan*

(Received 14 December 2010; published 11 March 2011)

Our study is focused on the relationship between the structural coherence and intrinsic carrier transport in a regioregular poly(3-hexylthiophene-2,5-diyl) (P3HT) nanofiber, particularly in an isolated nanofiber, formed in various ratios of good and poor solvent mixtures. The P3HT nanofiber, which is formed in solvent mixtures, had a whisker structure with the length of several μm, the height decreased from 9 to 2 nm as estimated by scanning force microscope observation, and the structural coherent length along the longitudinal axis increased from 40 to 59 Å as determined by x-ray-diffraction measurement, with increasing ratio of the good solvent. The *I-V* characteristics measured by the four-probe method showed that the activation energy of hopping conduction, which was considerably related with the structural disorder, decreased with increasing ratio of the good solvent. Moreover, the field-effect-transistor characteristics of the nanofiber showed that the carrier mobility increased with increasing ratio of the good solvent, and the nanofiber formed under the good-solvent-rich condition showed the mobility from 3.8×10^{-2} to 5.6×10^{-2} cm^2 V^{-1} s^{-1}. The tendency of the mobility to increase has been explained on the basis of the change in the structural coherent length and thermal activation energy, assuming the model that regarded the nanofiber as a one-dimensional array of electronically coherent regions and incoherent defects, and hence the relationship between the structural coherence and carrier transport has been clarified.

DOI: 10.1103/PhysRevB.83.115314 PACS number(s): 73.61.Ph, 72.80.Le, 73.63.Bd

I. INTRODUCTION

Recently, nanofibers have attracted increasing interest owing to their unique structure and properties, such as high aspect ratio, large specific surface area, and chemical/mechanical stabilities in various fields such as filtration, electronic devices, and sensors. In particular, the nanofiber with electronic function is expected to be used as building blocks for molecular electronics and conductive ink for printable electronics. Thus, conducting polymer nanofibers have been investigated for their potential applications in field-effect transistors (FETs).[1–3] The conducting polymer nanofiber can be prepared by various methods, such as template synthesis,[4–9] electrospinning,[10–18] dispersion with sonication,[19–24] molecular combing,[25,26] self-organization on a substrate or a liquid-air interface,[27–32] and whisker formation in a solution.[33–48]

To use these conducting polymer nanofibers as molecular wires for molecular electronics, the fibers fabricated by template synthesis and electrospinning are not suitable, because the typical thickness of these nanofibers is a few hundred nm, which is sufficiently thicker than the linewidth of semiconductor integrated circuits reduced to less than 32 nm nowadays. As a pioneering work of the thin nanofiber, Park and co-workers have reported that a polyacetylene nanofiber with the thickness of 20 nm showed the FET property, but the mobility of the isolated nanofiber was not so high, 4.4×10^{-5} cm^2 V^{-1} s^{-1} (Ref. 20). Therefore, we focused on the whisker-type nanofiber formed in a solution with the thickness of about 10 nm, which has great possibilities for wiring and functional materials for future electronic devices. The thin nanofiber obtained by whisker formation in a solution has been reported by Ihn *et al.*[33] By this method, the conducting polymer, regioregular poly(3-alkylthiophene) (rr-P3AT), was crystallized into well-defined whiskerlike entities from supercooled solutions in poor solvents such as cyclohexanone, prepared at 50 °C, by slowly cooling to room temperature, and the width and length of the whiskers were 15 nm and several μm, respectively. This method is quite simple and inexpensive; in addition, it has been reported that these nanofibers showed the FET effect.[35] After this research, FET measurement of this nanofiber has been intensively carried out in the thin-film state,[38,40–44,46] entangled network,[39,47] and isolated single fiber.[35,37,48] From these reports, it has been clarified that the nanofiber had a higher mobility than the nonfibrillar thin film[35,37–44,46–48] and had strong relation with alkyl chain length,[46,48] molecular weight,[42,44] and solvent using the crystallization.[38,40]

However, these phenomenological data do not provide us the indication to increase the mobility; hence, the relation between the mobility and structure, such as morphology or crystallinity, needs to be inspected. Here it is expected that the nanofiber structure, such as thickness, aspect ratio, and crystallinity, which is closely related with the electric properties, is controllable with changing conditions such as solvent, temperature, and cooling rate during the fiber formation. Therefore, in this study, our attention is directed to the relationship between the structure and carrier transport property of the regioregular poly(3-hexylthiophene-2,5-diyl) (rr-P3HT) nanofiber with the control of the structural coherence by changing the ratio of the solvent mixture during the nanofiber formation. We have investigated the electrical properties of the isolated state of various nanowires such as the insulated molecular wire made from polyaniline and cyclodextrin,[49]

the poly(3,4-ethylenedioxythiophene)/poly(styrenesulfonate) nanofiber,[25,26] DNA,[50] and the hexabenzocoronene nanotube[51] using fine electrodes with 100-200 nm spacing fabricated by scanning probe microscopy (SPM) lithography.[52–54] Furthermore, we have also applied this method to rr-P3HT nanofiber obtained by whisker formation by changing the alkyl chain length.[43,48] In this study, we aimed to relate the field-effect mobility with the structural coherence using the measurement method that we previously developed.

II. EXPERIMENTAL

A. Nanofiber preparation

rr-P3HT (Mw = 87 000) was purchased from Aldrich Co., Inc., and used without further purification. Conducting polymer nanofibers were prepared as follows:[33] rr-P3HT (25 mg) was added to the flask with an organic solvent mixture (50 g), and a 0.05 wt% P3HT solution was prepared by stirring at a high temperature (>70 °C). We used a solvent mixture of anisole as a poor solvent and chloroform as a good solvent at the ratios of 10:0, 8:2, 5:5, 3:7, and 2:8 v/v. Here, the value f was defined as the volume fraction of anisole; that is, we prepared the solvent mixtures of $f = 1.0$, 0.8, 0.5, 0.3, and 0.2, which was used as the index of the nanofiber crystallized in each solvent mixture in this paper. After the reflux was stopped, the solution was cooled gradually from 70 °C to 20 °C at a rate of 25 °C/h. The UV-visible absorption was determined using a UV-visible spectrometer V-630 (JASCO Co., Ltd.). The samples, which were used as undoped samples, were prepared in a N_2 atmosphere using a glove box and kept under vacuum for a few hours just before the measurement to avoid O_2 doping.

B. Measurement method

1. Structure characterization

The P3HT nanofibers were observed with a scanning force microscope (SFM) (CP-II, Veeco Instruments Inc.) in intermittent-contact SFM that was equipped with a commercial silicon cantilever with a spring constant and resonant frequency of 40 N/m and 300 KHz, respectively. For the SFM observation, the dispersion of the P3HT nanofiber was cast and dried by blowing air on a piece of Si wafer with a thermally grown SiO_2 layer on top, and the residual solvent on the substrate was removed by vacuum drying. The height of the nanofibers was determined from the cross sections of images that were perpendicular to the long axis of the nanofibers. Moreover, the thickness of the nanofiber was estimated by TEM measurement, where the nanofiber was put onto a carbon-coated Cu grid.

X-ray-diffraction (XRD) measurements were performed using an x-ray diffractometer (R-AXIS RAPID, Rigaku Co.) with an imaging-plate detector. For XRD measurement, P3HT nanofibers, collected by drying *in vacuo*, were placed in borosilicate glass capillary tubes (diameter, 1.5 mm; wall thickness, 0.01 mm) after being crushed into pieces. Since randomly oriented nanofibers showed a ringlike diffraction pattern, the diffraction pattern was converted into 2θ-intensity profiles using the Rigaku R-AXIS software, and then the 2θ-intensity profiles were corrected by subtracting the background intensity of the quartz capillary. The diffraction peak at 2θ in the 2θ-intensity profile was fitted using a Lorentzian function, which gave the full width at half maximum (FWHM) $\Delta\theta$ of the peak, where silicon-powder standard (supplied by National Institute of Standards and Technology) was used as a standard for compensation of linewidth ($\Delta\theta = 0.18^\circ$). The coherent length ξ, related with the characteristic length of the single-crystalline region along the normal direction of the 2θ plane, was estimated using the Scherrer equation as[45,55,56]

$$\xi = \frac{K\lambda}{\Delta\theta \cos\theta}, \tag{1}$$

where $K = 0.9$ is the Scherrer constant, and $\lambda = 1.542$ Å, the wavelength of Cu K_α radiation.

2. Electrical properties measurement

The substrate for the conductivity and FET measurements using four-probe Pt electrodes having a 200-nm gap was prepared on a piece of Si wafer with a thermally grown SiO_2 layer of ca. 255 nm thickness on top using photolithography in combination with SPM lithography according to the fabrication method reported by Hashizume and co-workers.[52–54] The spacing between the electrodes was determined to be 200 nm from the cross section of the SFM topographic image of the electrodes. The electrical isolation between electrodes was tested as a current of less than 0.2 pA at the applied voltage ranging from −1 to +1 V.

The substrate with electrodes was cleaned in a piranha solution (H_2SO_4: 30 wt% H_2O_2 aq. = 3 : 1 v/v) for 15 min at 45 °C. Then, the substrate surface was modified by dipping it in an octyltrimethylsilane solution (10 mmol/L in anhydrous hexane) for 10 min, followed by washing thrice with chloroform under N_2 atmosphere.

The conductivity measurement was carried out by a four-probe method in vacuum below 10^{-5} Torr from 300 K to 20 K using a combined system of a source/measure unit Keithley model 236 source measure unit (SMU) (Keithley Instruments, Inc.) for applying the current between the two outer electrodes and detecting the voltages of the two inner electrodes in a cryostat CRT-006 (Iwatani Industrial Gases Co., Ltd.). On the other hand, the FET measurement was carried out by a four-probe method in vacuum below 10^{-5} Torr at room temperature using a combined system of the cryostat CRT-006, the Keithley model 236 SMU for measuring the source-drain characteristics, and a Keithley 2400 digital sourcemeter (Keithley Instruments, Inc.) for applying the gate field.

III. RESULTS AND DISCUSSION

A. Nanofiber formation and structure characterization

The dissolution of P3HT in solvent mixtures produced a transparent orange solution at high temperatures (>70 °C). During cooling, solutions at the solvent ratio, anisole/chloroform, of 10:0, 8:2, and 5:5 v/v showed an obvious color change to purple, and accompanying this color change, two shoulders at about 550 and 600 nm appeared in addition to the main peak at 470–500 nm in the UV-visible absorption spectra. The solution at the solvent ratio,

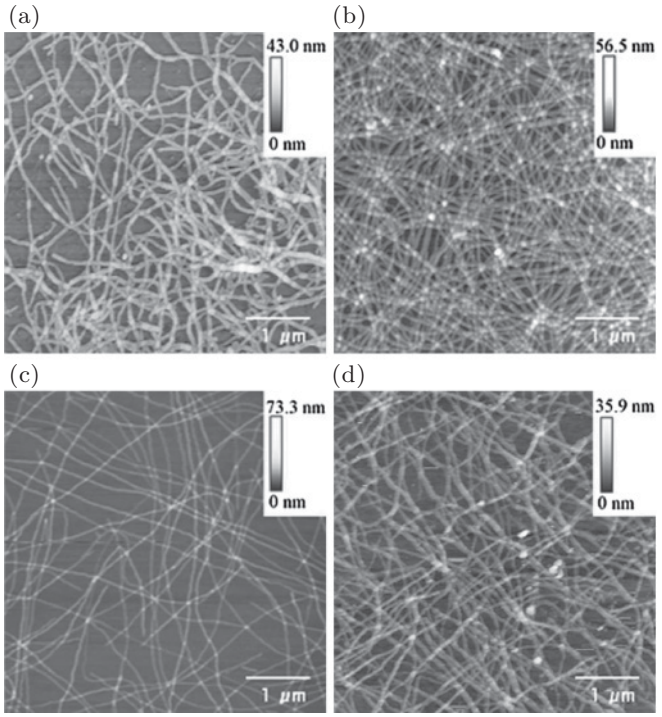

FIG. 1. SFM topographic images of nanofibers of f = (a) 1.0, (b) 0.8, (c) 0.5, and (d) 0.3.

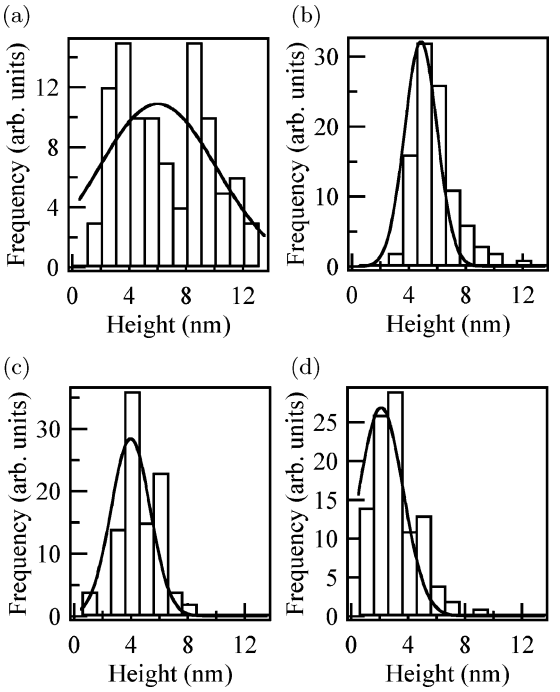

FIG. 2. Height histograms of nanofiber of f = (a) 1.0, (b) 0.8, (c) 0.5, and (d) 0.3 fitted by Gaussian function.

anisole/chloroform, of 3:7 v/v did not show any color change during cooling, but after two weeks at room temperature, the color changed to reddish brown and two shoulders at about 550 and 600 nm appeared in the UV-visible absorption spectrum. Furthermore, one-dimensional nanofibrillar structures were observed by SFM observation on the SiO_2/Si substrate, where each of the solutions showing color change was spin-coated. Figure 1 shows SFM topographic images in the scale of 5 × 5 μm. These images showed that the same structure to the whisker-type nanofiber previously reported[33] was crystallized in solution. In contrast, the solution at the solvent ratio, anisole/chloroform, of 2:8 v/v did not change color and no nanofibrillar structure was observed by SFM observation after a few weeks at room temperature.

Table I shows the average height h and standard deviation σ of nanofibers of f = 1.0–0.3, where each of them was estimated from arbitrary 100 nanofibers observed in SFM topographic images. σ was estimated from the height histogram of each nanofiber, as shown in Fig. 2, fitted by a Gaussian function. h increased from 2 to 6 nm with f, and hence, the thin nanofiber was obtained under the good-solvent-rich condition. Nanofibers of f = 0.8–0.3 had comparably uniform height, while nanofibers of f = 1.0 had a large standard deviation, which indicated the inhomogeneous morphology owing to the fast formation rate of the nanofibers.

TABLE I. Average height h and standard deviation σ of nanofiber with f estimated by SFM observation.

f	h (nm)	σ
1.0	6.00	4.14
0.8	4.89	1.15
0.5	3.97	1.37
0.3	2.10	1.54

From TEM analysis, the width d of the nanofiber, which was difficult to estimate from SFM images because of the tip locus effect, was estimated to be 15 nm. Taking into account both SFM and TEM results, the nanofiber had a rectangular shape with a high aspect ratio and oblong cross section, as suggested previously.[35,37] According to this model, a P3HT nanofiber consisted of folded or extended polymer backbones stacked along the nanofiber longitudinal axis and of laminated layers of the polymer backbones separated by hexyl side chains. A schematic illustration of a nanofiber structure model is shown in Fig. 3.

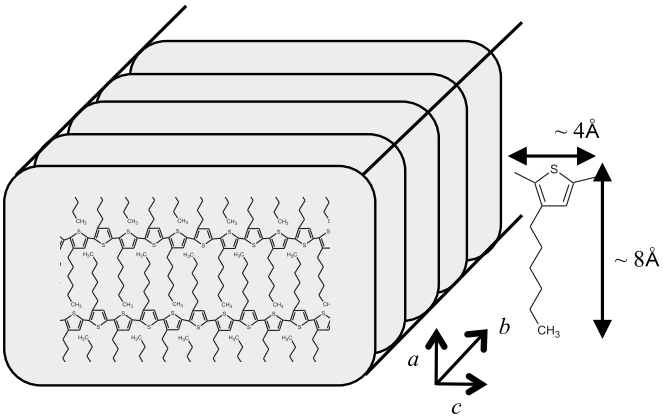

FIG. 3. Schematic diagram of the structure model of nanofiber. The lamellae of polymer chains in the ac plane are stacking to the b axis, which corresponds to the longitudinal axis of nanofibers, by π-π interaction.

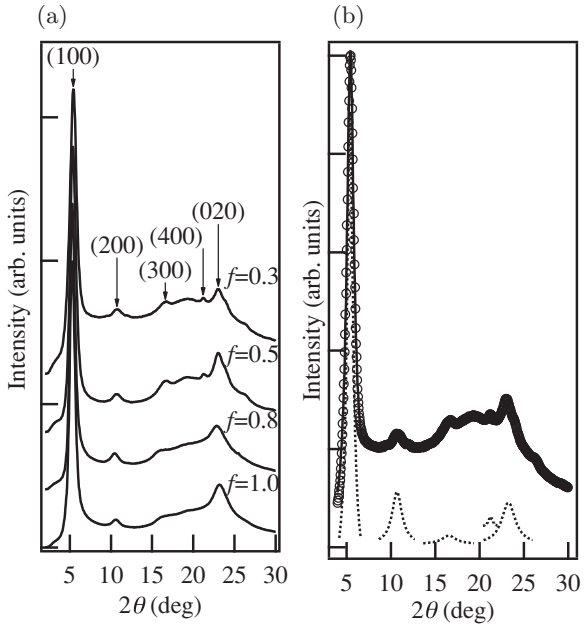

FIG. 4. (a) X-ray diffraction of nanofibers with changing f. (b) X-ray diffraction of nanofiber of $f = 0.3$ fitted by the sum of Lorentzians corresponding to each peak component: x-ray diffraction data (open circles), fitting curve (solid line), peak component (dotted line). The baseline and broad peak at $2\theta \approx 20^\circ$ used in a fitting function are not shown for simplicity.

The nanofibers were analyzed by x-ray diffraction to investigate the internal structure, as shown in Fig. 4(a). Two main peaks and a few small peaks were confirmed in each sample, suggesting that the nanofiber consisted of a crystalline structure. The peak angle 2θ, possible index, and interlayer distance d are summarized in Table II. The peak angles of both peaks were nearly independent of f, and hence the fundamental crystal structure did not change with the solvent condition during nanofiber formation. The peak at $2\theta \approx 5.3^\circ$ indicated the periodic structure of the a axis (the height direction) in Fig. 3, since the corresponding interlayer distance of the (100) diffraction, $d_{100} \approx 17$ Å, has almost the same value as the sum of twice the molecular length of the hexyl chains on all-trans conformation tilted and the width of a polythiophene backbone. The higher-order peaks of (200), (300), and (400) were confirmed in the diffraction of the nanofiber, $f = 0.5$ and 0.3; in contrast, only the peaks of (200) and (300) were recognized as higher-order peaks in the diffraction of the nanofiber, $f = 1.0$ and 0.8. This tendency indicated that the crystalline orders of the nanofiber, $f = 0.5$ and 0.3, that is, the fibers crystallized under good-solvent-rich condition, were higher than those of the nanofiber, $f = 1.0$ and 0.8.

On the other hand, the peak at $2\theta \approx 23^\circ$ indicated the periodic structure of the b axis (the longitudinal direction) in Fig. 3, since the corresponding interlayer distance of the (020) diffraction, $d_{020} \approx 3.8$ Å, has almost the same value as the stacking of the polymer chain by π-π interaction between the polymer backbones.

The diffraction data was fitted by the sum of Lorentzians corresponding to each peak component as shown in Fig. 4(b), which was the case of $f = 0.3$ as an example, and the FWHM $\Delta\theta$ and the standard deviation σ were estimated. The baseline and broad peak at $2\theta \approx 20^\circ$ used in a fitting function were not shown in Fig. 4(b) for simplicity. $\Delta\theta$, σ, and the coherent length ξ estimated using the Scherrer equation are shown in Table III. The coherent length ξ_{020} of the b axis decreased clearly from 59.3 to 39.8 Å with f. Since the coherent length is strongly related with the size of the crystal grain in the nanofiber, the result indicates that the crystallinity along the b axis, the longitudinal axis of the nanofiber, decreases with f, that is, the good-solvent-rich condition. In addition, the coherent length of a single-crystalline order is expected to affect the carrier transport property along the nanofiber.

TABLE II. Peak angle 2θ, possible index, and interlayer distance d of the nanofiber with f estimated by x-ray diffraction.

f	2θ (deg)	Index	d (Å)
1.0	5.31	(100)	16.6
	10.40	(200)	8.51
	16.31	(300)	5.44
	23.31	(020)	3.82
0.8	5.33	(100)	16.6
	10.28	(200)	8.61
	15.82	(300)	5.60
	22.98	(020)	3.87
0.5	5.39	(100)	16.4
	10.51	(200)	8.42
	16.49	(300)	5.38
	21.40	(400)	4.15
	23.24	(020)	3.83
0.3	5.44	(100)	16.2
	10.30	(200)	8.59
	16.62	(300)	5.33
	21.20	(400)	4.19
	23.21	(020)	3.83

The solubility of P3HT is dependent on the hexyl side chain, while the crystallization is due to the π-π interaction of the polythiophene main chain. Therefore, the nanofiber formation occurs because of the competition between the dissolubility of the alkyl side chain and the π-π interaction of the polythiophene main chain. With decreasing temperature, the dissolubility of hexyl side chains decreased and it promoted the π-π stacking, and polymers turned out to form nanofibers. Since the value of the Hildebrand solubility parameter (SP) δ of anisole, chloroform, and P3HT were 9.5, 9.2, and 9.1 $\text{cal}^{1/2}\ \text{cm}^{-3/2}$ (Ref. 57), respectively, no nanofiber appeared at room temperature when the SP value of solvent δ_{sol} was under ca. 9.27 ($f = 0.2$) calculated from the proportional

TABLE III. The FWHM $\Delta\theta$, the standard deviation σ, and the coherent length ξ estimated by Scherrer equation corresponding to the peak (020) of nanofiber with f.

f	$\Delta\theta$ (deg)	σ	ξ (Å)
1.0	2.04	0.07	39.8
0.8	2.12	0.23	38.3
0.5	1.67	0.08	48.6
0.3	1.37	0.06	59.3

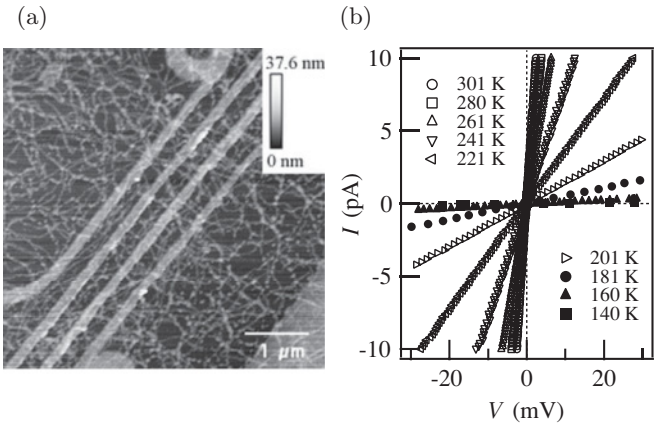

FIG. 5. (a) SFM topographic image of nanofibers of $f = 0.3$ on electrodes with gaps of 200 nm. (b) I-V profiles of nanofibers of $f = 0.3$ with varying temperature from 301 K to 140 K.

distribution of each molar fraction. Nanofibers appeared at δ_{sol} of more than 9.30 ($f > 0.3$) at room temperature, and then with δ_{sol} approaching 9.5, the acceleration of the fiber growth rate led to an amorphous aggregation and crystal defects, which were observed as the decrease in the coherent length and the increase in the nanofiber height.

B. Conductivity estimation of an isolated nanofiber

I-V characteristics of the nanofiber without doping at various temperatures were measured by the four-probe method. Figure 5(a) shows the SFM topographic image of the nanofiber of $f = 0.3$, positioned across the fine electrodes with the gap of 200 nm, and Fig. 5(b) shows the I-V profiles of the nanofiber of $f = 0.3$ with varying temperature from 301 K to 140 K. In this temperature region, profiles could be explained on the basis of Ohmic behavior.

Conductivity σ is estimated as

$$\sigma = \frac{G \cdot l}{n \cdot S}, \tag{2}$$

where G is the conductance, n is the number of nanofibers bridged between four electrodes counted from SFM images, S is the section area of nanofiber estimated from SFM and TEM images, and l is the length between electrodes of 200 nm. The conductivities of the nanofiber of $f = 1.0$, 0.8, 0.5 and 0.3 were estimated to be 9.2×10^{-6}, 3.2×10^{-4}, 4.7×10^{-4}, and 4.3×10^{-4} S/cm, respectively, at room temperature.

With decreasing temperature, the conductivity markedly decreased; that is, semiconducting-type behavior was observed. Figure 6 shows the Arrhenius plots of the conductivity of the nanofiber of $f = 1.0$, 0.8, 0.5, and 0.3. The plots gave an approximately linear relationship in the temperature region above 140 K, and hence, it was found that the carrier transport in nanofibers had the thermal activation property as follows:

$$\sigma = \sigma_0 \exp\left(-\frac{\Delta E}{k_B T}\right), \tag{3}$$

where ΔE is the activation energy of carrier transport. By fitting the experimental data with Eq. (3) (the solid lines in Fig. 6), the activation energy of nanofibers was estimated, as

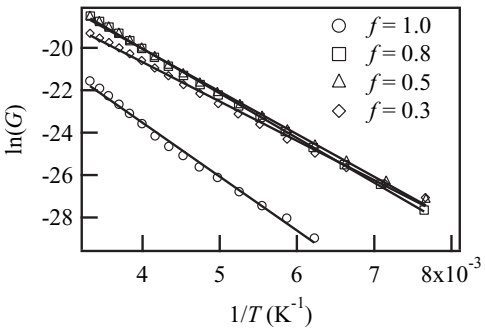

FIG. 6. Arrhenius plots of the conductance of nanofibers, $f = 1.0$, 0.8, 0.5, and 0.3, where solid lines show the fitting plot with a linear relationship.

shown in Table IV. Since the activation energy decreased with f, the smaller barrier with carrier transport in nanofibers was realized in the nanofiber crystallized under good-solvent-rich condition, and the result seems to be consistent with the structural characterization by XRD analysis. Although the activation energy estimated from the conductance may include both that of the carrier excitation and that of the hopping on carrier transport, the result that the activation energy strongly depends on f indicated that the former is not dominant.

C. Carrier mobility estimation of an isolated nanofiber by FET measurement

1. Thin-film state of entangled nanofibers

The FET property of nanofibers was measured by the four-probe method (200-nm gap) using the bottom gate configuration in the thin-film state of entangled nanofibers at room temperature. In this measurement, nanofibers covered the electrodes uniformly at a high density, and the channel length and width were assumed to be the gap between electrodes and the effective width of electrodes, respectively. Figure 7 shows the transfer characteristics of nanofibers, $f = 1.0$, 0.8, 0.5 and 0.3, at fixed $V_{SD} = -5$ V, which was the value within the region where the I_{SD}-V_{SD} curves obeyed a linear relationship (Ohmic law) on the output characteristics, while sufficient saturation was not observed at the measured region of V_{SD}, which was limited by avoiding the exfoliation of electrodes. The typical p-type property was observed, for example, in the case of $f = 0.3$; the remarkable amplification of I_{SD} with respect to negative gate voltage V_G led to the $I_{SD} \sim 0.1$ μA at the V_G of -40 V. The I_{SD} increased linearly in the low negative V_G region below about -25 V and then tended to saturate above -40 V.

Table V summarizes the parameters estimated from these characteristics: field-effect mobility μ, threshold voltage V_{th},

TABLE IV. Thermal activation energy ΔE of nanofibers with f estimated from temperature dependence of conductivity.

f	ΔE (meV)	f	ΔE (meV)
1.0	231	0.5	173
0.8	182	0.3	160

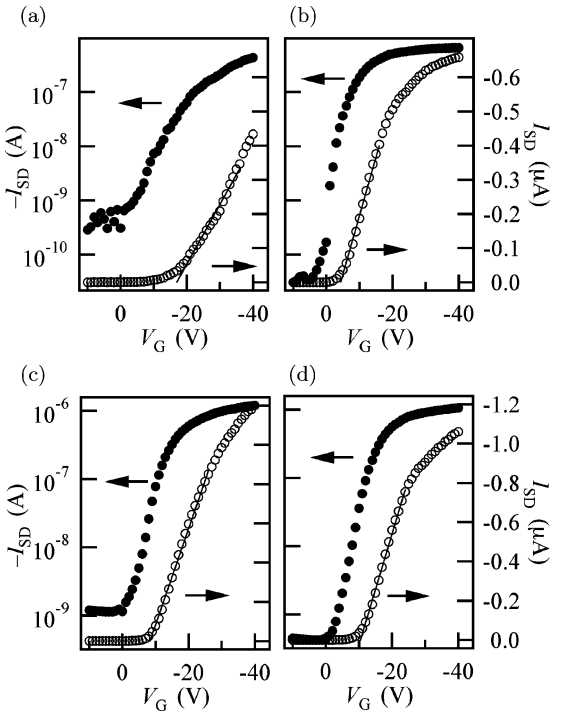

FIG. 7. Transfer characteristics of nanofibers of f = (a) 1.0, (b) 0.8, (c) 0.5, and (d) 0.3 at room temperature ($V_{SD} = -5$ V), where solid lines show the fitting characteristic with a linear relationship.

and on-off ratio I_{on}/I_{off}. The field-effect mobility μ was estimated from the linear regime using the following relationship:

$$I_{SD} = \frac{W}{L}\mu C_{ox} V_{SD}(V_G - V_{th}), \tag{4}$$

where L (=200 nm) is the spacing of electrodes, W (=5 m) is the effective width of electrodes, and C_{ox} is the oxide capacitance per unit area of the SiO_2 insulating layer (thickness, 255 nm), estimated to be 13.8 nF/cm^2. Here, since nanofibers fully covered the surface between electrodes from the SFM observation, we used the width of electrodes as the channel width without considering the surface coverage of nanofibers.

Since the field-effect mobility increased with f as shown in Table V, the larger carrier mobility in nanofibers was realized in the nanofiber crystallized under good-solvent-rich condition, and the result also seems to be consistent with the structural characterization by XRD analysis. Namely, the larger the structural coherent length of the nanofiber, the larger the mobility it shows.

TABLE V. Field-effect mobility μ, threshold voltage V_{th}, and on-off ratio I_{on}/I_{off} of nanofiber with f estimated from the transfer characteristics.

f	μ (cm^2 V^{-1} s^{-1})	V_{th} (V)	I_{on}/I_{off}
1.0	1.0×10^{-2}	−17.0	1.4×10^3
0.8	2.0×10^{-2}	4.4	3.9×10^3
0.5	2.8×10^{-2}	−8.3	1.1×10^3
0.3	3.3×10^{-2}	−10.5	2.4×10^3

The field-effect mobility μ obtained in this study was of the same order as that reported previously in the case of the P3HT nanofiber, namely, 1.0×10^{-2}–6.0×10^{-2} cm^2 V^{-1} s^{-1} (Refs. 35, 37–44, 46–48). In comparison with that of the thin film of P3HT, typically 5.0×10^{-3}–3.0×10^{-2} cm^2 V^{-1} s^{-1} (Refs. 58–62), the nanofiber tends to have a larger mobility than the thin film. Since the nanofiber formation process, that is, the whisker formation process, generally excludes impurities or amorphous regions and achieves a well-organized microstructure, a higher mobility of the nanofiber is acceptable. However, in the film state of entangled nanofibers, both ends of nanofibers do not always come into contact with electrodes, and there are fibers getting caught with the electrode at one end and another nanofiber at the other end. Therefore, the effect of the interfibrillar carrier transport cannot be eliminated from the electric properties; hence, the field-effect mobility should be decreased. Thus, we measured the FET of an isolated nanofiber.

2. Isolated nanofiber

The FET property of a completely isolated nanofiber was measured by the four-probe method (200-nm gap) using a bottom gate configuration at room temperature. In this measurement, we put a few nanofibers on electrodes. Figure 8 shows the SFM topographic images of nanofibers, f = 1.0, 0.8, 0.5, and 0.3, on electrodes, where the schematic images of nanofibers on electrodes are inserted at the upper right of the SFM images, and Fig. 9 shows the transfer characteristics of the nanofibers, f = 1.0, 0.8, 0.5, and 0.3, at fixed $V_{SD} = -5$ V, which was the value within the region where the I_{SD}-V_{SD} curves obeyed a linear relationship (Ohmic law) on the output characteristics. The remarkable amplification of I_{SD} with respect to the negative gate voltage V_G was observed in every case; for example, $f = 1.0$ led to the $I_{SD} \sim 1.6$ nA at the V_G of −40 V, while sufficient saturation was not observed at the measured region of V_G.

From SFM topographic images, the numbers of nanofibers bridged across all four electrodes n_{14} of f = 1.0, 0.8, 0.5, and 0.3 were 1, 1, 3, and 4, respectively, which were used for the estimation of the channel width, while there were nanofibers that bridged only two center electrodes for voltage sensing (the electrode indexes 2 and 3 in Fig. 8), and if these nanofibers contributed to the carrier transport, the channel width should be estimated from the numbers of nanofibers that bridged two electrodes for sensing, n_{23}, of f = 1.0, 0.8, 0.5, and 0.3, which were 2, 1, 4, and 6, respectively. Which one should be used depended on the contributions of two dominant factors for the carrier transport: the carrier injection from metal to the nanofiber and the carrier transport in the nanofiber. In FET measurement, the former is included in the contact resistance and the latter corresponds to the intrinsic resistance of the nanofiber. Since in this study we adopted the four-probe method, the contact resistance between the electrodes and the nanofibers bridged across all four electrodes was neglected to the some extent, but that on the nanofibers that bridged two center electrodes was considered. As a result, the relation between the effective mobility estimated from the

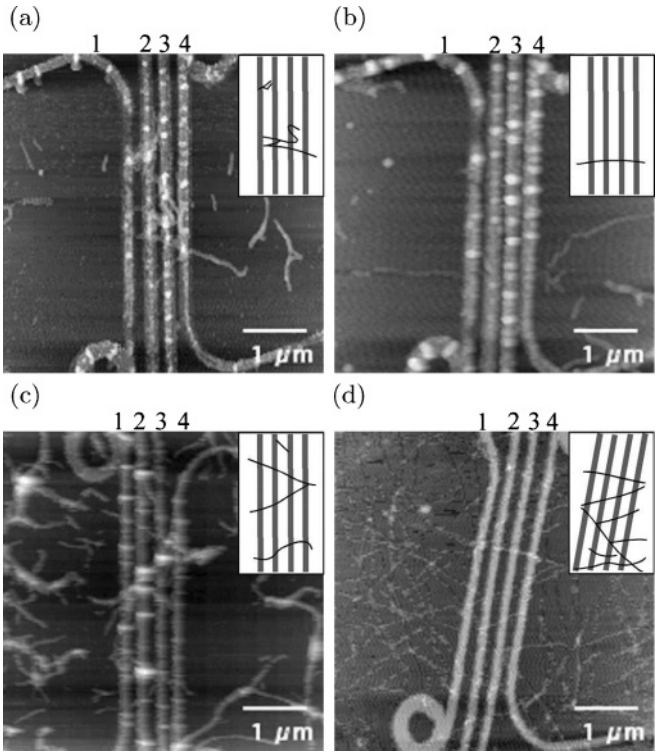

FIG. 8. SFM topographic images of nanofibers of $f =$ (a) 1.0, (b) 0.8, (c) 0.5, and (d) 0.3 on electrodes. The numbers of nanofibers of $f = 1.0$, 0.8, 0.5, and 0.3 bridged across four electrodes were 1, 1, 3, and 4, respectively.

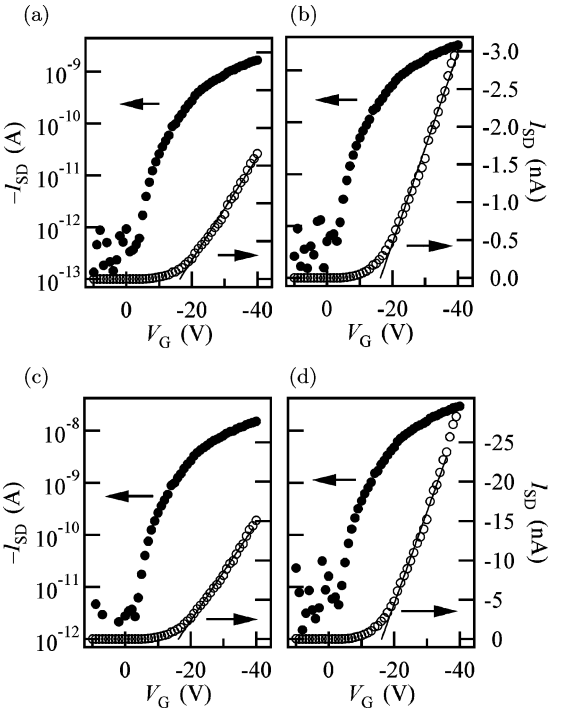

FIG. 9. Transfer characteristics of a few nanofibers, $f =$ (a) 1.0, (b) 0.8, (c) 0.5, and (d) 0.3, at room temperature ($V_{SD} = -5$ V), where solid lines show the fitting characteristic with a linear relationship.

transfer characteristics in the linear regime μ^* and the intrinsic mobility of the isolated nanofiber μ was expressed as[63]

$$\mu^* \frac{W}{L} C_{ox}(V_G - V_{th}) = \mu \frac{n_{14} w}{L} C_{ox}(V_G - V_{th}) + \left\{ \left[\mu \frac{(n_{23} - n_{14})w}{L} C_{ox}(V_G - V_{th}) \right]^{-1} + 2R_c \right\}^{-1}. \quad (5)$$

Here R_c is the contact resistance of the carrier pass from a nanofiber through electrodes to another nanofiber, and $w =$ 15 nm is the width of a nanofiber. Furthermore, we assumed that V_{th} was independent of respective nanofibers.

At first, in the case that the contact resistance is sufficiently large (Case 1),

$\{\mu(n_{23} - n_{14})wC_{ox}(V_G - V_{th})/L\}^{-1} \ll R_c$, Eq. (5) is approximately written as

$$\mu^* \frac{W}{L} C_{ox}(V_G - V_{th}) = \mu_{14}^{I} \frac{n_{14} w}{L} C_{ox}(V_G - V_{th}). \quad (6)$$

Since a large potential energy is needed to inject carriers to the nanofiber, nanofibers that bridged only two center electrodes for voltage sensing do not serve us the carrier path, and hence, we estimated the field-effect mobility μ_{14}^{I} in an isolated nanofiber, as shown in Table VI.

Next, considering the case that the contact resistance is sufficiently negligible (Case 2), $\{\mu(n_{23} - n_{14})wC_{ox}(V_G - V_{th})/L\}^{-1} \ll R_c$, Eq. (5) is approximately written as

$$\mu^* \frac{W}{L} C_{ox}(V_G - V_{th}) = \mu_{23}^{I} \frac{n_{23} w}{L} C_{ox}(V_G - V_{th}). \quad (7)$$

Since the carrier injection from electrodes to nanofibers occurs without any potential energy, nanofibers that bridged only two center electrodes for voltage sensing also carry current, and an effective channel width is enlarged; hence, the field-effect mobility μ_{23}^{I} was estimated and shown in Table VI. Consequently, the intrinsic field-effect mobility of an isolated nanofiber should be in the range from μ_{23}^{I} to μ_{14}^{I}.

In addition, for example, in the case of $f = 0.3$, there were nanofibers that bridged aslant electrodes and these nanofibers, which had a larger effective resistance, carried smaller current than those that bridged perpendicularly. Thus, an effective channel length can be larger than L and then the mobility tended to be underestimated. Thus, as a maximum value, the field-effect mobility μ_{14}^{II} considering the channel length l_i of each nanofiber in Case 1 was estimated and shown in Table VI using the following relation:

$$\mu^* \frac{W}{L} C_{ox}(V_G - V_{th}) = \sum_{i=1}^{n_{14}} \frac{w}{l_i} \mu_{14}^{II} C_{ox}(V_G - V_{th}). \quad (8)$$

To confirm the reproducibility, we checked the mobility in the case of $f = 0.3$ while varying the number of nanofibers on the electrodes. In the case of $n_{14} = 7$, $n_{23} = 9$, μ_{14}^{I} and μ_{23}^{I} were estimated to be 4.8×10^{-2} cm^2 V^{-1} s^{-1} and 3.7×10^{-2} cm^2 V^{-1} s^{-1}, respectively, and the values were quite similar to those of $f = 0.3$ in Table VI. From the result, it was found that the nanofiber formed under the same conditions had similar mobilities as determined by the local property measurement.

The mobility of the isolated nanofiber tended to be higher than that of the film, except for the nanofiber of $f = 1.0$, even

TABLE VI. Various parameters of FET consisting of a few nanofibers and the mobility of an isolated nanofiber with f estimated from the transfer characteristics. n_{14} and n_{23} are numbers of nanofibers that bridge all electrodes and center electrodes for sensing. μ^{I}_{14}, μ^{I}_{23}, and μ^{II}_{14} are field-effect mobilities in Case 1, Case 2, and Case 1 considering the channel length of each nanofiber, respectively. V_{th} and $I_{\mathrm{on}}/I_{\mathrm{off}}$ are the threshold voltage and on-off ratio, respectively.

f	n_{14}	n_{23}	μ^{I}_{14} (cm^2 V^{-1} s^{-1})	μ^{I}_{23} (cm^2 V^{-1} s^{-1})	μ^{II}_{14} (cm^2 V^{-1} s^{-1})	V_{th} (V)	$I_{\mathrm{on}}/I_{\mathrm{off}}$
1.0	1	2	1.3×10^{-2}	6.5×10^{-3}	1.5×10^{-2}	−16.4	1.8×10^{3}
0.8	1	1	2.4×10^{-2}	2.4×10^{-2}	2.4×10^{-2}	−16.3	2.1×10^{3}
0.5	3	4	4.0×10^{-2}	3.0×10^{-2}	5.4×10^{-2}	−16.2	1.7×10^{3}
0.3	4	6	5.6×10^{-2}	3.8×10^{-2}	6.1×10^{-2}	−16.1	1.8×10^{3}

if on the minimum value μ^{I}_{23}. The result is acceptable since an isolated nanofiber does not have a crosstalk pathway, which makes the mobility decrease, and therefore, in the nanofiber of $f = 1.0$, which has many defects in the crystal structure, the advantage of the isolation can be lost. In addition, it was one of the reasons the effective channel width of the film state was overestimated, because the channel width was used as the width of the electrodes W, which was not necessarily effective all over the width of the electrodes with some parts not in contact with nanofibers.

3. *Relation between coherent length and field-effect mobility*

In the case of both the film state and the isolated state, the field-effect mobility of the nanofiber decreased with f, and, hence, carrier transport with high mobility was realized in the nanofiber crystallized under good-solvent-rich condition. This result was consistent with the structural characterization by XRD analysis; that is, it was indicated that a higher mobility was derived from the longer structural coherent length. Although the structural coherent length is not necessarily equivalent to the electronic coherent length, both lengths should be closely related because they are ascribed to the length strongly affected by the crystal structure in the nanofiber.

Here, we regard the nanofiber as a one-dimensional array of electronically coherent regions corresponding to the crystal regions with the carrier mobility μ_0 and incoherent defects such as crystal defects or amorphous structures with the mobility $\mu_1 = \mu_0 \exp(-\Phi/k_{\mathrm{B}}T)$. The length of the coherent region and the thickness of defects are defined as l_0 and d_0,

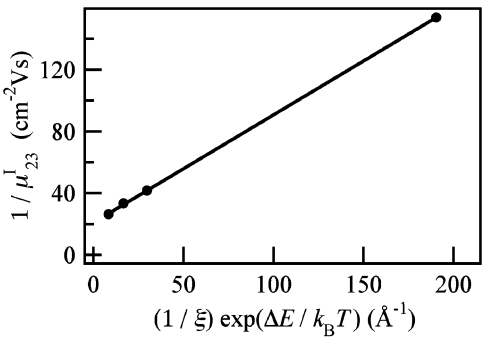

FIG. 10. $1/\mu^{\mathrm{I}}_{23}$ plotted against $(1/\xi)\exp(\Delta E/k_{\mathrm{B}}T)$ to confirm the model of the average mobility, where solid lines show the fitting one with linear relationship.

respectively. The average mobility of carrier conduction $\bar{\mu}$ can be written as

$$\frac{1}{\bar{\mu}} = \frac{l_0/\mu_0 + d_0/\mu_1}{(l_0 + d_0)} \approx \frac{1}{\mu_0}\left\{1 + \frac{d_0}{l_0}\exp(\Phi/k_{\mathrm{B}}T)\right\}, \quad (9)$$

because this array can be regarded as the series of resistances proportional to l_0/μ_0 and d_0/μ_1. In addition, the nanofiber has fundamentally the whisker structure, and the incoherent defect is assumed to be a kind of dislocation rather than the amorphous region, where the size of defect d_0 is independent of f and not so large, $l_0 \gg d_0$. We assume that Φ corresponds to the activation energy ΔE derived from the temperature dependence of the conductivity. ΔE includes the contribution of both the carrier hopping and the carrier activation, but since the conducting polymer is in the saturation region of impurity semiconductor by residual dopants rather than the intrinsic region, the assumption is not so irrelevant. Furthermore, since l_0 should be related with the structural coherent length ξ, we assume that they have a linear relation, that is, $l_0 = \alpha\xi$. Figure 10 shows $1/\mu^{\mathrm{I}}_{23}$ plotted against $(1/\xi)\exp(\Delta E/k_{\mathrm{B}}T)$, and the characteristics obeyed the linear relation, which is consistent with Eq. (9). This result that the mobility data was explained properly using this model indicates that the structural coherence is linearly related with the electrical coherence, which determine the carrier mobility. In addition, on μ^{I}_{14}, no linear relationship according to Eq. (9) was obtained. From Fig. 10, we can obtain the μ_0 of μ^{I}_{23} as a y intercept to be 4.7×10^{-2} cm^2 V^{-1} s^{-1} by fitting with the linear function. μ_0 corresponds to the highest mobility, which is the value obtained after removing completely the incoherent defect from the nanofiber. This mobility is not the highest but a sufficiently higher level than that reported previously in the case of rr-P3HT nanofiber.[35,37–44,46–48] Hence, the control of the nanofiber structure, particularly crystallininty, is an indispensable factor for obtaining high mobility. Finally, in this nanofiber structure, the carrier conduction is attributable to not the intramolecular conduction in the π-conjugation system but almost to the intermolecular conduction of π-π stacking. By theoretical calculation, Lan *et al.* have reported that this interchain hole mobility in the P3AT nanofiber was approximately 10^{-2} cm^2 V^{-1} s^{-1}, which was two orders of magnitude smaller than that of the intrachain mobility.[64] The realization of the highest mobility much for silicon may need a nanofiber with another structural design using the intramolecular carrier conduction instead of the intermolecular one.

IV. SUMMARY

We have investigated the relationship between the structural coherence, which was studied by XRD measurement, and the carrier transport, which was obtained by conductivity and FET measurements of an isolated nanofiber while changing the condition of the nanofiber formation. As a result, the nanofiber formed under the good-solvent-rich condition showed a high mobility of from 3.8×10^{-2} to 5.6×10^{-2} cm^2 V^{-1} s^{-1}, and the carrier mobility had a strong relationship with the structural coherent length. The model of the nanofiber as a one-dimensional array of electronically coherent regions and incoherent defects can explain the data properly, and the mobility of the nanofiber with the incoherent defect completely removed was expected to be 4.7×10^{-2} cm^2 V^{-1} s^{-1} at a moderate estimation. Since the nanofiber used the π-π stacking as a carrier path, the realization of the highest mobility for silicon may require the intramolecular π conjugation using another structural design.

ACKNOWLEDGMENTS

This work was partially supported by a Grant-Aid for Scientific Research (B) (Grant No. 20350102) and a Grant-in-Aid on Priority Area "Soft Matter Physics" (Grant No. 18068015) from the Ministry of Education, Culture, Sports, Science and Technology of Japan.

*To whom correspondence should be addressed: simo@cc.tuat.ac.jp

[1] A. P. H. J. Schenning and E. W. Meijer, Chem. Commun. 3245 (2005).
[2] A. N. Aleshin, Phys. Solid State **49**, 2015 (2007).
[3] A. L. Briseno, S. C. B. Mannsfeld, S. A. Jenekhe, Z. Bao, and Y. Xia, Mater. Today **11**, 38 (2008).
[4] C. R. Martin, Science **266**, 1961 (1994).
[5] C. R. Martin, Acc. Chem. Res. **28**, 61 (1995).
[6] K. Kim and J. I. Jin, Nano Lett. **1**, 631 (2001).
[7] J. G. Park, S. H. Lee, B. Kim, and Y. W. Park, Appl. Phys. Lett. **81**, 4625 (2002).
[8] J. Joo, B. H. Kim, D. H. Park, H. S. Kim, D. S. Seo, J. H. Shim, S. J. Lee, K. S. Ryu, K. Kim, J. I. Jin, T. J. Lee, and C. J. Lee, Synth. Met. **153**, 313 (2005).
[9] G. A. O'Brien, A. J. Quinn, D. Iacopino, N. Pauget, and G. Redmond, J. Mater. Chem. **16**, 3237 (2006).
[10] I. D. Norris, M. M. Shaker, F. K. Ko, and A. G. MacDiarmid, Synth. Met. **114**, 109 (2000).
[11] A. G. MacDiarmid, W. E. Jones, I. D. Norris, J. Gao, A. T. Johnson, N. J. Pinto, J. Hone, B. Han, F. K. Ko, H. Okuzaki, and M. Llaguno, Synth. Met. **119**, 27 (2001).
[12] A. G. MacDiarmid, Angew. Chem. Int. Ed. **40**, 2581 (2001).
[13] N. J. Pinto, A. T. Johnson, A. G. MacDiarmid, C. H. Mueller, N. Theofylaktos, D. C. Robinson, and F. A. Miranda, Appl. Phys. Lett. **83**, 4244 (2003).
[14] N. J. Pinto, A. T. Johnson, A. G. MacDiarmid, C. H. Mueller, N. Theofylaktos, D. C. Robinson, and F. A. Miranda, Appl. Phys. Lett. **83**, 4244 (2003).
[15] Y. X. Zhou, M. Freitag, J. Hone, C. Staii, A. T. Johnson, N. J. Pinto, and A. G. MacDiarmid, Appl. Phys. Lett. **83**, 3800 (2003).
[16] D. Li, A. Babel, S. A. Jenekhe, and Y. N. Xia, Adv. Mater. **16**, 2062 (2004).
[17] H. Q. Liu, C. H. Reccius, and H. G. Craighead, Appl. Phys. Lett. **87**, 253106 (2005).
[18] I. S. Chronakis, S. Grapenson, and A. Jakob, Polymer **47**, 1597 (2006).
[19] G. T. Kim, M. Burghard, D. S. Suh, K. Liu, J. G. Park, S. Roth, and Y. W. Park, Synth. Met. **105**, 207 (1999).
[20] J. G. Park, G. T. Kim, V. Krstic, B. Kim, S. H. Lee, S. Roth, M. Burghard, and Y. W. Park, Synth. Met. **119**, 53 (2001).
[21] A. N. Aleshin, H. J. Lee, Y. W. Park, and K. Akagi, Phys. Rev. Lett. **93**, 196601 (2004).
[22] A. N. Aleshin, H. J. Lee, S. H. Jhang, H. S. Kim, K. Akagi, and Y. W. Park, Phys. Rev. B **72**, 153202 (2005).
[23] A. N. Aleshin, Adv. Mater. **18**, 17 (2006).
[24] H. J. Lee, Z. X. Jin, A. N. Aleshin, J. Y. Lee, M. J. Goh, K. Akagi, Y. S. Kim, D. W. Kim, and Y. W. Park, J. Am. Chem. Soc. **126**, 16722 (2004).
[25] S. Samitsu, T. Iida, M. Fujimori, S. Heike, T. Hashizume, T. Shimomura, and K. Ito, Synth. Met. **152**, 497 (2005).
[26] S. Samitsu, T. Shimomura, K. Ito, M. Fujimori, S. Heike, and T. Hashizume, Appl. Phys. Lett. **86**, 233103 (2005).
[27] P. Samori, I. Sikharulidze, V. Francke, K. Mullen, and J. P. Rabe, Nanotechnology **10**, 77 (1999).
[28] T. Bjornholm, T. Hassenkam, D. R. Greve, R. D. McCullough, M. Jayaraman, S. M. Savoy, C. E. Jones, and J. T. McDevitt, Adv. Mater. **11**, 1218 (1999).
[29] Z. M. Zhang, Z. X. Wei, and M. X. Wan, Macromolecules **35**, 5937 (2002).
[30] W. P. Hu, H. Nakashima, K. Furukawa, Y. Kashimura, K. Ajito, and K. Torimitsu, Appl. Phys. Lett. **85**, 115 (2004).
[31] D. H. Kim, Y. D. Park, Y. Jang, S. Kim, and K. Cho, Macromol. Rapid Commun. **26**, 834 (2005).
[32] G. H. Lu, L. G. Li, and X. N. Yang, Adv. Mater. **19**, 3594 (2007).
[33] K. J. Ihn, J. Moulton, and P. Smith, J. Polym. Sci., Part B: Polym. Phys. **31**, 735 (1993).
[34] S. Malik and A. K. Nandi, J. Polym. Sci., Part B: Polym. Phys. **40**, 2073 (2002).
[35] J. A. Merlo and C. D. Frisbie, J. Polym. Sci., Part B: Polym. Phys. **41**, 2674 (2003).
[36] N. Kiriy, E. Jahne, H. J. Adler, M. Schneider, A. Kiriy, G. Gorodyska, S. Minko, D. Jehnichen, P. Simon, A. A. Fokin, and M. Stamm, Nano Lett. **3**, 707 (2003).
[37] J. A. Merlo and C. D. Frisbie, J. Phys. Chem. B **108**, 19169 (2004).
[38] J. F. Chang, B. Q. Sun, D. W. Breiby, M. M. Nielsen, T. I. Solling, M. Giles, I. McCulloch, and H. Sirringhaus, Chem. Mater. **16**, 4772 (2004).
[39] M. Mas-Torrent, D. den Boer, M. Durkut, P. Hadley, and A. P. H. J. Schenning, Nanotechnology **15**, S265 (2004).
[40] H. C. Yang, T. J. Shin, L. Yang, K. Cho, C. Y. Ryu, and Z. N. Bao, Adv. Funct. Mater. **15**, 671 (2005).
[41] D. H. Kim, Y. Jang, Y. D. Park, and K. Cho, J. Phys. Chem. B **110**, 15763 (2006).

[42]R. Zhang, B. Li, M. C. Iovu, M. Jeffries-EL, G. Sauve, J. Cooper, S. J. Jia, S. Tristram-Nagle, D. M. Smilgies, D. N. Lambeth, R. D. McCullough, and T. Kowalewski, J. Am. Chem. Soc. **128**, 3480 (2006).
[43]S. Samitsu, T. Shimomura, S. Heike, T. Hashizume, and K. Ito, Macromolecules **41**, 8000 (2008).
[44]J. H. Liu, M. Arif, J. H. Zou, S. I. Khondaker, and L. Zhai, Macromolecules **42**, 9390 (2009).
[45]W. D. Oosterbaan, V. Vrindts, S. Berson, S. Guillerez, O. Douheret, B. Ruttens, J. D'Haen, P. Adriaensens, J. Manca, L. Lutsen, and D. Vanderzande, J. Mater. Chem. **19**, 5424 (2009).
[46]W. D. Oosterbaan, J. C. Bolsee, A. Gadisa, V. Vrindts, S. Bertho, J. D'Haen, T. J. Cleij, L. Lutsen, C. R. McNeill, L. Thomsen, J. V. Manca, and D. Vanderzande, Adv. Funct. Mater. **20**, 792 (2010).
[47]M. Arif, J. H. Liu, L. Zhai, and S. I. Khondaker, Appl. Phys. Lett. **96**, 243304 (2010).
[48]S. Samitsu, T. Shimomura, S. Heike, T. Hashizume, and K. Ito, Macromolecules **43**, 7891 (2010).
[49]T. Shimomura, T. Akai, M. Fujimori, S. Heike, T. Hashizume, and K. Ito, Synth. Met. **153**, 497 (2005).
[50]A. Inomata, T. Shimomura, S. Heike, M. Fujimori, T. Hashizume, and K. Ito, J. Phys. Soc. Jpn. **75**, 074803 (2006).
[51]J. P. Hill, W. S. Jin, A. Kosaka, T. Fukushima, H. Ichihara, T. Shimomura, K. Ito, T. Hashizume, N. Ishii, and T. Aida, Science **304**, 1481 (2004).
[52]M. Ishibashi, S. Heike, and T. Hashizume, Jpn. J. Appl. Phys. **39**, 7060 (2000).
[53]M. Kato, M. Ishibashi, S. Heike, and T. Hashizume, Jpn. J. Appl. Phys. **41**, 4916 (2002).
[54]T. Akai, T. Abe, T. Shimomura, M. Kato, M. Ishibashi, S. Heike, B. K. Choi, T. Hashizume, and K. Ito, Jpn. J. Appl. Phys. **42**, 4764 (2003).
[55]A. L. Patterson, Phys. Rev. **56**, 978 (1939).
[56]C. Yang, F. P. Orfino, and S. Holdcroft, Macromolecules **29**, 6510 (1996).
[57]E. A. Grulke, in *Polymer Handbook*, 4th ed., edited by J. Brandrup, E. H. Immergut, and E. A. Grulke (Wiley, New York, 1999), Vol. 2, Chap. 7, p. 675.
[58]Z. N. Bao, Y. Feng, A. Dodabalapur, V. R. Raju, and A. J. Lovinger, Chem. Mater. **9**, 1299 (1997).
[59]K. Kaneto, W. Y. Lim, W. Takashima, T. Endo, and M. Rikukawa, Jpn. J. Appl. Phys. **39**, L872 (2000).
[60]A. Babel and S. A. Jenekhe, Synth. Met. **148**, 169 (2005).
[61]A. Zen, M. Saphiannikova, D. Neher, U. Asawapirom, and U. Scherf, Chem. Mater. **17**, 781 (2005).
[62]Y. D. Park, D. H. Kim, Y. Jang, J. H. Cho, M. Hwang, H. S. Lee, J. A. Lim, and K. Cho, Org. Electron. **7**, 514 (2006).
[63]C. Reese and Z. Bao, Adv. Funct. Mater. **19**, 763 (2009).
[64]Y. K. Lan, C. H. Yang, and H. C. Yang, Polym. Int. **59**, 16 (2010).